nature materials

SUPPLEMENTARY INFORMATION

DOI: 10.1038/NMAT3755

Ultrathin conformal devices for precise and continuous thermal characterization of human skin

R. Chad Webb[1†], Andrew P. Bonifas[1†], Alex Behnaz[2], Yihui Zhang[3,4], Ki Jun Yu[5], Huanyu Cheng[4], Mingxing Shi[6], Zuguang Bian[4,7], Zhuangjian Liu[8], Yun-Soung Kim[1], Woon-Hong Yeo[1], Jae Suk Park[5], Jizhou Song[9], Yuhang Li[4], Yonggang Huang[4], Alexander M. Gorbach[2], John A. Rogers[1]*

[1]Department of Materials Science and Engineering, University of Illinois at Urbana-Champaign, Urbana, IL 61801, USA
[2]National Institute of Biomedical Imaging and Bioengineering, National Institutes of Health, Bethesda, MD 20892, USA
[3]Center for Mechanics and Materials, Tsinghua University, Beijing 100084, P.R. China
[4]Department of Civil and Environmental Engineering and Department of Mechanical Engineering, Northwestern University, Evanston, IL 60208, USA
[5]Department of Electrical and Computer Engineering, University of Illinois at Urbana-Champaign, Urbana, IL 61801, USA
[6]School of Mechanics and Engineering, Southwest Jiaotong University, Chengdu 610031, P.R. China
[7]Ningbo Institute of Technology, Zhejiang University, Ningbo 315100, P.R. China
[8]Institute of High Performance Computing, 1 Fusionopolis Way, #16-16 Connexis, Singapore 138632
[9]Department of Mechanical and Aerospace Engineering, University of Miami, Coral Gables, Florida 33146, USA

†These authors contributed equally to this work

*To whom correspondence should be addressed: E-mail: jrogers@illinois.edu

Supplementary Note 1: Fabrication procedure for 4 x 4 TCR sensor arrays

Prepare polymer base layers

1. Clean a 3” Si wafer (Acetone, IPA -> Dry 5 min at 110 °C).
2. Spin coat with PMMA (poly(methyl methacrylate), spun at 3,000 rpm for 30 s).
3. Anneal at 180 °C for 1 min.
4. Spin coat with polyimide (PI, poly(pyromellitic dianhydride-co-4,4′ -oxydianiline), amic acid solution, Sigma-Aldrich, spun at 4,000 rpm for 30 s).
5. Anneal at 110 °C for 30 s.
6. Anneal at 150 °C for 5 min.
7. Anneal at 250 °C under vacuum for 1 hr.

Deposit first metallization

8. E-beam 5/40 nm Cr/Au.
9. Pattern photoresist (PR; Clariant AZ5214, 3000 rpm, 30s) with 365 nm optical lithography through iron oxide mask (Karl Suss MJB3).
   Develop in aqueous base developer (MIF 327).
10. Etch Au with TFA Au etchant (Transene).
11. Etch Cr with CR-7 Cr Mask Etchant (Cyantek).
12. Remove PR w/ Acetone, IPA rinse.
13. Dry 5 min at 150 °C.

Isolate first metallization and pattern via holes

14. Spin coat with PI.
15. Anneal at 110 °C for 30 s.
16. Anneal at 150 °C for 5 min.
17. Anneal at 250 °C under vacuum for 1 hr.
18. Pattern photoresist (PR; Clariant AZ4620, 3000 rpm, 30s;) with 365 nm optical lithography through iron oxide mask (Karl Suss MJB3).
    Develop in aqueous base developer (AZ 400K, diluted 3:1).
19. Reactive ion etch (RIE; March CS-1701, 50 mTorr, 20 sccm O2, 150 W, 35 min).

Deposit second metallization

20. E-beam 5/200 nm Cr/Au.
21. Pattern PR AZ5214.
22. Etch Au with TFA Au etchant.
23. Etch Cr with Cr Mask Etchant.
24. Remove PR w/ Acetone, IPA rinse.
25. Dry 5 min at 150 °C.

Isolate entire device

26. Spin coat with PI.
27. Anneal at 110 °C for 30 s.
28. Anneal at 150 °C for 5 min.
29. Anneal at 250 °C under vacuum for 1 hr.
30. Pattern PR AZ4620.
31. RIE (50 mTorr, 20 sccm O2, 150 W, 35 min).

Release and transfer

32. Release w/ boiling Acetone.
33. Transfer to PDMS stamp.
34. E-beam 3/30 nm Ti/SiO2.
35. Transfer to ~50 µm silicone sheet.
36. Bond thin, flexible cable (Elform, HST-9805-210) using hot iron with firm pressure

Supplementary Note 2: Fabrication procedure for 8 x 8 PIN sensor arrays

p+ doping

1. Clean a 320 nm SOI wafer (acetone, IPA, water, drying at 110°C for 5 min).
2. Clean by Buffer Oxide Etch (BOE) 6:1 for 1 min.
3. Deposit Plasma Enhanced Chemical Vapor Deposition (PECVD; Plasmatherm SLR730) SiO_2 900 nm.
4. Clean the wafer (acetone, IPA, water, drying at 110°C for 5min).
5. Treat with HMDS for 3 min.
6. Pattern PR (p+ doping).
7. Anneal at 110°C for 5 min.
8. Etch oxide in RIE (CF_4: 40 sccm, O_2: 1.2 sccm, 150W, 59 mTorr) for 30 min.
9. Etch residual oxide in BOE (NH_4F:HF=10:1) for 2 min.
10. Remove PR by acetone
11. Clean by RCA 1 and RCA 2 for 10 min each
12. Dip in BOE for 10 sec
13. Expose to diffusive boron source at 1000°C for 25 min.
14. Clean the processed wafer (HF 1min, RCA 1 for 10 min, RCA 2 for 10 min BOE 1 min).

n+ doping

15. Deposit PECVD SiO2 500 nm.
16. Clean the wafer (acetone, IPA, water, drying at 110°C for 5 min).

17. Treat with HMDS for 3 min.
18. Pattern PR (n+ doping).
19. Anneal at 110°C for 5 min.
20. Etch oxide in RIE (CF_4: 40 sccm, O_2: 1.2 sccm, 150W, 59 mTorr) for 20 min.
21. Etch residual oxide in BOE (NH_4F:HF=10:1) for 1.5 min.
22. Remove PR by acetone
23. Clean by RCA 1 and RCA 2 for 10 min each
24. Dip in BOE for 10 sec
25. Expose to diffusive phosphorus source at 1000°C for 7 min.
26. Clean the processed wafer (HF 1min, RCA 1 for 10min, RCA 2 for 10 min BOE 1 min).

Oxide layer etching in SOI wafer

27. Pattern PR (3 μm pitch dot patterns).
28. Etch silicon by RIE (50mTorr, 40sccm SF6, 100W, 1 min).
29. Etch buried oxide layer of SOI wafer via dot patterns in HF for 30 min.

Substrate preparation

30. Spin coat with PMMA on the substrate (additional wafer, 3000 rpm 30 s).
31. Anneal at 180 °C for 3 min.
32. Spin coat with PI (4000 rpm, 60 s).
33. Aneal at 110 °C for 40 s.

Transfer printing

34. Release Si layer with PDMS stamp from SOI wafer.
35. Print Si layer onto prepared substrate.
36. Anneal at 150°C for 4 min.
37. Remove PR by acetone and IPA.
38. Aneal at 250°C for 1 h under vacuum.

Silicon Isolation

39. Pattern PR.
40. Etch silicon by RIE (50 mTorr, 40 sccm SF_6, 100 W, 1 min)
41. Remove PR by acetone and IPA.

Pattern 1st via hole

42. Deposit PECVD SiO_2 100 nm.
43. Pattern PR (holes).
44. Open via holes with BOE for 1 min.

45. Remove PR by acetone and IPA.

Deposit 1st Metallization

46. E-beam 10/100 nm Cr/Au.
47. Pattern PR.
48. Wet etch Cr/Au.
49. Remove PR by acetone and IPA.

Isolate 1st layer and Pattern 2nd via hole

50. Spin coat with PI (4000 rpm, 60 s).
51. Anneal at 110°C for 3min at 150°C for 10 min.
52. Anneal at 250°C for 2 h under vacuum.
53. Pattern PR.
54. Etch via holes by RIE (O_2: 20 sccm, 200W, 150 mTorr) for 10 min.
55. Remove PR by acetone and IPA.

Deposit 2nd Metallization

56. E-beam 10/700 nm Cr/Au.
57. Pattern PR.
58. Wet etch Cr/Au.
59. Remove PR by acetone and IPA.

Isolate 2st layer and Pattern 3nd via hole

60. Spin coat with PI (4000 rpm, 60 s).
61. Anneal at 110°C for 3 min at 150°C for 10 min.
62. Anneal at 250°C for 2 h under vacuum.
63. Pattern PR.
64. Etch via holes by RIE (20 sccm O_2, 200 W, 150 mTorr) for 10 min.
65. Remove PR by acetone and IPA.

Deposit 3rd Metallization

66. E-beam 10/300 nm Cr/Au.
67. Pattern PR.
68. Wet etch Cr/Au.
69. Etch 3rd PI layer by RIE (20 sccm O_2, 200 W, 150 mTorr) for 5 min.
70. Pattern PR for ACF opening.
71. Wet etch Cr/Au.
72. Remove PR by acetone and IPA.
73. Release and transfer

74. Bond thin, flexible cable (Elform, HST-9805-210) using hot iron with firm pressure

Supplementary Note 3: Temperature measurements and calibrations

Temperature measurements of the TCR devices are recorded via a National Instruments PXI-6289 board with custom electronics programmed with LabVIEW software with all 16 channels recorded simultaneously at a 15 ms sampling time. The probe current employed to measure resistance was selected to be 160 μA to avoid self-heating of the sensors, confirmed to be less than 0.02 °C with IR thermometry, while maximizing signal to noise. A 16 bit A/D converter, an input range of ±200 mV, and a 160 μA probe current has 0.04 Ω bin sizes resulting in a bin size of 0.02 °C at our sampling frequency of 66.67 Hz. The sampling frequency was limited by the data transfer speed of the laptop computer.

Temperature sensor calibrations are performed by applying the devices to an aluminum plate, painted matte black, and set on a hot plate. For the TCR device, the hot plate is set to one of six temperature points from 25 °C – 50 °C, allowed to stabilize for 10 min, and then the resistances of all 16 sensors are recorded for 60 seconds. The temperature is recorded using an IR thermometer, and the resistance value for each sensor is given as the average of each sensor's 60 second recording. This measurement is repeated for a total of six temperature points from 25 °C – 50 °C and is used to generate the calibration curves shown in Supplementary Figure S2a. The 16 curves are separated into four groups of four, each group separated by a small resistance constant, due to the difference in interconnect length for each of the 4 rows. A typical value for the resistance change of a sensor due to temperature is 1.9 - 2 $\Omega\cdot°C^{-1}$, as shown in Supplementary Figure S2a. This resistance change corresponds to a TCR value of 2.5×10^{-3} $°C^{-1}$, which is lower than the reported bulk Au value of 3.7×10^{-3} $°C^{-1}$. Thin metallic layers typically have lower TCR compared to their bulk material owing to a large constituent of temperature independent resistance caused by surface scattering[1]. The generated calibration equation for each sensor is then applied to future measurements to convert resistance readings to temperature. Typical data points during a 150 s measurement period on the bench and on skin are shown in Supplementary Figure S2d-e, respectively. When data is averaged from 66.67 Hz to 2 Hz, which is shown in Supplementary Figure S2d-e, the standard deviations of the temperature readings over the 150 s periods are 0.012 °C and 0.021 °C for the sensor on the hot plate and on skin, respectively. If the data is averaged from 66.67 Hz to 0.5 Hz, the standard deviations drop to 0.008 °C and 0.014 °C on the hot plate and skin, respectively. It was observed that the absolute accuracy of the sensors would sometimes vary between experiments while maintaining the same temperature sensitivity, which would manifest itself in a constant offset in temperature reading. This is attributed to small variations in the contact resistance between the sensor contact pads and heat bonded cable used to connect to the data acquisition system. Because the sensors rely on a measurement of voltage drop through the circuit, a change in the contact resistance of the wire leads should manifest as a constant offset in temperature reading. This change was typically <5 °C over a period of months, and could be alleviated by the use of 4-point resistance measurements, or wireless data transmission in the future. To account for the potential constant resistance offset, the temperature reading of each sensor was compared to the IR camera reading at a single instance in time, and the difference was applied as a constant to each sensor's calibration equation. This was deemed reasonable because the data of interest is precise temperature changes over time, as opposed to absolute temperature accuracy.

PIN devices were measured and calibrated in the same fashion as the TCR devices, but with a different data acquisition system. PIN diodes were measured using an Agilent 4155C parameter analyzer to measure the voltage drop at forward biased current levels of 10 μA and 20 μA, which show corresponding sensitivities of 2.34 $\mathrm{mV\cdot °C^{-1}}$ and 2.44 $\mathrm{mV\cdot °C^{-1}}$ respectively (Supplementary Fig. S2b-c). Individual diodes can be addressed in the array in a multiplexed format by picking the proper row and column external contacts to apply bias, allowing current to only flow through a single diode at any given time in a format that allows for rapid switching.

Supplementary Note 4: Strain effects

Finite element analysis (FEA) was used to study the effect of device strain on both the TCR and PIN based temperature sensors. For the TCR device, the sensors were assumed to be perfectly bonded to the elastomeric substrate for modeling purposes. An applied uniaxial strain of 10% was applied in the longitudinal direction at the upper end of the substrate while the lower end was clamped. The substrate was modeled by the hexahedron element C3D8R; the sensor arrays were modeled by the composite shell element S4R in the ABAQUS finite element program. The strains in the TCR elements in the longitudinal and horizontal directions shown in Supplementary Figure S5b-c indicate small variation across the width direction of each TCR element. Each TCR element can be taken as many small resistors connecting in parallel in the width direction followed by a series connection in the length direction. Small variation of the strain in the width direction allows us to approximate the parallel connection with an average calculation, which leads to a simplified expression of the relative resistance change $\Delta R/R = \left(1+\varepsilon_{length}\right)/\left(1+\varepsilon_{width}\right)-1$, where ε_{length} and ε_{width} are the average strains in the length and width directions, respectively. This approximation gives the upper bound of the resistance change, which is confirmed with the comparison to the experiment as shown in Supplementary Figure 5d.

Unlike TCR devices with increased interconnect lengths of progressive sensor rows, the PIN device appears in a periodic mesh layout, which simplifies our analysis to a unit cell containing only one diode in the finite element analysis. Periodic boundary conditions were applied to ensure that each unit cell neither overlaps nor form gaps with adjacent cells, while a uniaxial 10% strain was applied. Element type selections are the same as described in the analysis for TCR device. Because silicon diodes are off from the neutral mechanical plane of the device, bending was induced even though only uniaxial strain was applied, as supported by the strain profiles at the top and bottom surfaces of Si diode in Supplementary Figure S6.

Supplementary Note 5: Thermal load on skin

The thermal mass of the devices are determined for two practical constructions: with and without a 50 μm silicone supporting substrate. The devices have an overall aerial coverage of ~4 cm^2. The calculated thermal masses that follow are given as thermal mass per unit area of skin. The device construction for the TCR device contains approximately 120 $\mu\mathrm{g\cdot cm^{-2}}$ of Au, 90 $\mu\mathrm{g\cdot cm^{-2}}$ of PI, and, for the case with a 50 μm silicone backing, 5 $\mathrm{mg\cdot cm^{-2}}$ of silicone support (calculated values). The material contributions to aerial thermal mass are: 15 $\mu\mathrm{J\cdot cm^{-2}\cdot K^{-1}}$ from Au, 125 $\mu\mathrm{J\cdot cm^{-2}\cdot K^{-1}}$ from PI, and 7 $\mathrm{mJ\cdot cm^{-2}\cdot K^{-1}}$ from the silicone backing (calculate values). This resulting overall device aerial thermal masses are 150 $\mu\mathrm{J\cdot cm^{-2}\cdot K^{-1}}$ for the case with no silicone support, and 7.2 $\mathrm{mJ\cdot cm^{-2}\cdot K^{-1}}$ for the case of a 50 μm silicone support. The PIN system has a denser device coverage, with resulting aerial thermal mass of approximately 500 $\mu\mathrm{J\cdot cm^{-2}\cdot K^{-1}}$ for the case with no silicone support, and 7.6 $\mathrm{mJ\cdot cm^{-2}\cdot K^{-1}}$ for the case with the silicone support. The thermal mass of skin depends on the water content where thermal mass increases with skin hydration and water content[2]. For hydrated skin, the heat capacity is approximately 3.7 $\mathrm{J\cdot cm^{-3}\cdot K^{-1}}$, and the device aerial thermal mass (no support) of 120 $\mu\mathrm{J\cdot cm^{-2}\cdot K^{-1}}$ is equivalent to the aerial thermal mass of skin with a thickness of 320 nm (320 nm skin thickness times 3.7 $\mathrm{J\cdot cm^{-3}\cdot K^{-1}}$ volumetric heat capacity equals 120 $\mu\mathrm{J\cdot cm^{-2}\cdot K^{-1}}$). For the PIN system with the silicone support (largest thermal mass), where the thermal mass is 7.6 $\mathrm{mJ\cdot cm^{-2}\cdot K^{-1}}$, the device thermal mass is equal to a skin thickness of 21 μm.

Supplementary Note 6: Water vapor permeability

In order to minimize the effect of the devices on skin hydration, the devices can be applied directly to skin with no supporting substrate, as discussed in the main text. In this case, the sensors are effectively a largely void mesh on the skin, leaving the majority of the skin in the region of the sensors open to air allowing for normal water vapor transport from the skin. In the cases where a silicone support is used for robustness, the 50 μm thick silicone sheet has a small impact on skin hydration (Supplementary Fig. S8c) which results in a 5% (n = 6, range = 2.8% – 9.5%) change in skin hydration after 3 hours of continuous use on the forearm as measured by a commercially available impedance-based skin hydration sensor (Delfin MoistureMeterSC). This change in skin hydration appears to have minimal, if any, impact on long-term temperature measurements. Supplementary Figure S8b shows two sets of temperature readings from the IR camera throughout 70 min of mental stimulus experiment. One set is taken from a region through the sensor system, and the other is taken adjacent to the sensors (Supplementary Fig. S8a). During the first half of the experiment, the maximum difference in temperature reading is 0.3 °C, which could be the result of non-uniform temperature changes in the hand. It should also be noted that the readings taken through the sensor patch always result in a lower IR temperature reading, when they occur, and may be due to the lower emissivity of the sensor system causing a slight decrease in IR temperature reading. During the second half of the experiment, there is a larger difference in reading between regions, likely due to real non-unformities in the temperature change of the hand.

Supplementary Note 7: Sensor response time

As shown in Supplementary Figure S7a, a TCR element is embedded in a PI layer (of thickness H_{PI}) on top of a layer of solaris silicone elastomer (of thickness $H_{solaris}$). The TCR element in the experiment is very thin (e.g., ~50 nm) and has thermal conductivity and diffusivity (the ratio of thermal conductivity to volumetric heat capacity) much larger (> 1600 times) than the PI such that its effect on thermal analysis of the system can be neglected. The TCR element is at a distance d below the top surface.

A warm ethylene glycol drop (or skin) on top of the PI layer heats up the entire system. The in-plane dimensions of the PI layer are much larger than its thickness such that the heat flux is mainly along the thickness direction, which can be represented by a one-dimensional heat transfer model

$$\frac{\partial T}{\partial t} - \alpha \frac{\partial^2 T}{\partial x^2} = 0 \tag{1}$$

where T is the temperature increase (from the ambient temperature), α is the thermal diffusivity, and the coordinate x is along the thickness direction. The warm ethylene glycol (or skin) provides a constant temperature increase T_0 at the top,

$$T\big|_{x=0} = T_0 . \tag{2}$$

The numerical analysis suggests that the natural convection at the bottom surface of solaris has a negligible effect and can be approximated by a thermal isolation condition[3]

$$\left.\frac{\partial T}{\partial x}\right|_{x=H_{PI}+H_{solaris}}=0\,. \tag{3}$$

In addition, the temperature and heat flux, $-k\partial T/\partial x$, are continuous across the PI/solaris interface, where k is the thermal conductivity. The initial condition is

$$\left.T\right|_{t=0}=0\,. \tag{4}$$

The Laplace transform is used to solve Eqs. (1)-(4). The transformed temperature can be expanded into series. The temperature of the sensor, T_{sensor}, which is the same as the temperature of the PI at the same position *x*=*d*, can then be obtained by the inverse Laplace transform as

$$T_{sensor}=T_0\sum_{n=0}^{\infty}\sum_{m=0}^{n}(-1)^m C_n^m\varphi^{n-m}\sum_{l=0}^{n-m}C_{n-m}^{l}\left\langle\begin{array}{l} erfc\left\{\left[(n-l+1)\nu+m+l+1-\mu/2\right]H_{PI}\Big/\sqrt{\alpha_{PI}t}\right\} \\ -\varphi erfc\left\{\left[(n-l)\nu+m+l+1-\mu/2\right]H_{PI}\Big/\sqrt{\alpha_{PI}t}\right\} \\ +erfc\left\{\left[(n-l)\nu+m+l+\mu/2\right]H_{PI}\Big/\sqrt{\alpha_{PI}t}\right\} \\ -\varphi erfc\left\{\left[(n-l+1)\nu+m+l+\mu/2\right]H_{PI}\Big/\sqrt{\alpha_{PI}t}\right\} \end{array}\right\rangle \tag{5}$$

where $C_n^m=\dfrac{n!}{m!(n-m)!}$, $\varphi=\dfrac{k_{solaris}/\sqrt{\alpha_{solaris}}-k_{PI}/\sqrt{\alpha_{PI}}}{k_{solaris}/\sqrt{\alpha_{solaris}}+k_{PI}/\sqrt{\alpha_{PI}}}$, $\nu=\dfrac{H_{solaris}}{H_{PI}}\sqrt{\dfrac{\alpha_{PI}}{\alpha_{solaris}}}$, $\mu=d/H_{PI}$, and *erfc* is the complementary error function[4].

The thermal properties of PI and solaris are $k_{PI}=0.12\ \mathrm{W/(m\cdot K)}$, $\alpha_{PI}=7.75*10^{-8}\mathrm{m^2/s}$ [5], $k_{solaris}=0.186\ \mathrm{W/(m\cdot K)}$ and $\alpha_{solaris}=1.08*10^{-7}\mathrm{m^2/s}$ [6] (from manufacturer), which give $\varphi=0.135$. For such a small φ and a much larger thickness of the solaris layer (e.g., $H_{solaris}=60\mu\mathrm{m}$) than the PI layer (e.g., $H_{PI}=3.6$ or $6.0\mu\mathrm{m}$) in experiments, Eq. (5) can be simplified to

$$T_{sensor}=T_0\left\{\begin{array}{l} erfc\left(\dfrac{\mu}{2}\dfrac{H}{\sqrt{\alpha_{PI}t}}\right)+erfc\left[\left(\nu+1-\dfrac{\mu}{2}\right)\dfrac{H}{\sqrt{\alpha_{PI}t}}\right]-erfc\left[\left(\nu+1+\dfrac{\mu}{2}\right)\dfrac{H}{\sqrt{\alpha_{PI}t}}\right] \\ +\varphi erfc\left[\left(1+\dfrac{\mu}{2}\right)\dfrac{H}{\sqrt{\alpha_{PI}t}}\right]-\varphi erfc\left[\left(1-\dfrac{\mu}{2}\right)\dfrac{H}{\sqrt{\alpha_{PI}t}}\right] \end{array}\right\} \tag{6}$$

The sensor response time is defined by the time at which the sensor temperature increase T_{sensor} reaches 90% of T_0. For $H_{PI}-d=1.2\mu\mathrm{m}$ and $H_{solaris}=60\mu\mathrm{m}$ as in the experiment, the sensor response time is 3.7 ms for $H_{PI}=3.6\mu\mathrm{m}$ and 13.1 ms for $H_{PI}=6.0\mu\mathrm{m}$. These agree reasonably well with the experimentally measured sensor response time (for T_{sensor} = $0.9T_0$) of 4.2 ms and 12.2 ms for $H_{PI}=3.6$ and $6.0\mu\mathrm{m}$, respectively.

Supplementary Note 8: Fourier analysis of temperature readings

Low frequency temperature oscillations were examined via Fourier transforms of temperature signals obtained by the TCR device, as well as the IR camera, on the ventral forearm. For the TCR device, the readings of each of the 16 elements in the TCR device were averaged to generate a one-dimensional time-domain signal. This signal was then resampled with a resampling factor of 3/100. This brought the original sample rate of 66.67 Hz (15 ms sample period) to 2 Hz to match the sample rate of the IR camera. The resampled data were then subjected to a digital elliptical filter with a cutoff frequency of 0.004 Hz. The outcome of this filtering operation had the filter startup transients removed, and was then subjected to FFT analysis. For the IR camera, the readings of each pixel in the ROI were averaged to generate a one-dimensional time-domain signal. The signal was then subjected to same elliptical filter and analysis as the TCR device signals. In order to verify that the prominent frequency peaks are physiologically generated and not measurement artifacts due to the electronics of the TCR device, control experiments were run under the same conditions as the epidermal oscillations test (see Methods), but with the TCR device placed on a black felt pad instead of human skin. The results, compared to the results from human skin, are shown in Supplementary Figure S8d and show that dominant peaks present on skin are absent on the felt pad.

Supplementary Note 9: Mathematical modeling of reactive hyperemia

A two-dimensional heat transfer model was developed to determine the time-dependent temperature distribution in the tissues surrounding the artery during and after occlusion. A schematic illustration of the tissue geometry appears in Supplementary Figure S10, where a circular cross section is adopted for the wrist to simplify the analyses. The blood at body temperature flows through the circular artery embedded in the subcutaneous layer (mainly composed of fat), and heats the surrounding tissues. The heat exchange between the blood flow and the fat layer across the artery wall is modeled via a heat convection model[7], which linearly correlates the exchanged heat flux with the blood flow rate in the form of

$$q = \bar{h}_{artery-wall}\left(T_{body} - T_s\right) = \frac{\rho_b c_{pb} \omega_b(t)}{\pi D_{artery}}\left(T_{body} - T_s\right), \tag{7}$$

where q is the heat flux flowing into the fat layer; ρ_b, c_{pb}, $\omega_b(t)$ are the density, specific heat capacity, and time-dependent flow of the blood; D_{artery} is the diameter of the artery; T_{body} and T_s are the body temperature, and the temperature of fat at the artery wall, respectively; $\bar{h}_{artery-wall}$ is the equivalent heat transfer coefficient. Due to the heating from blood flow, the temperature redistributes in the surrounding tissues, which follows the temporal heat conduction equation of $\rho_j c_j \frac{\partial T_j}{\partial t} = k_j \left(\frac{\partial^2 T_j}{\partial x^2} + \frac{\partial^2 T_j}{\partial y^2} + \frac{\partial^2 T_j}{\partial z^2} \right)$ (j=1..4), where the subscript represents different tissues (with skin as j=1, fat as j=2, muscle as j=3, and bone as j=4). The free, outer surface of the skin has natural convection with air, which usually cools down the skin due to a lower room temperature than body temperature.

The solution of the heat transfer model includes two steps, which starts from the simulation of the steady-state heat conduction in the various tissues due to constant heating of blood flow, corresponding to the stage of pre-occlusion (Stage I). Then, by using the steady-state solution as an input, we further simulate the temporal variation of temperature in the tissues due to the application and release of occlusion, corresponding to the stage of vascular occlusion (Stage II) and reperfusion (Stage III), respectively. The blood perfusion keeps constant during Stage I, and varies with time during Stages II and III. Based on previous experimental data[6], the temporal variation of blood flow during these different stages can be well described by the following piecewise function[7,8]

$$
\begin{aligned}
&\omega_b^{I}(t) = \omega_0, \; t \le t_{occ,st} \\
&\omega_b^{II}(t) = (\omega_0 - \omega_s)\exp(-t/\tau_0) + \omega_s, \; t_{occ,st} < t \le t_{occ,end} \\
&\omega_b^{III}(t) = \begin{cases} (\omega_{\max} - \omega_s)\sin^2\left[\pi(t - t_{occ,end})/(2t_{dw})\right] + \omega_s, \; t_{occ,end} < t \le (t_{occ,end} + t_{dw}) \\ (\omega_{\max} - \omega_f)\exp\left[-(t - t_{occ,end} - t_{dw})/\tau_h\right] + \omega_0, \; t > (t_{occ,end} + t_{dw}) \end{cases}
\end{aligned}
\tag{8}
$$

where ω_0 represents the baseline blood flow and has the same value as that of the healthy tissue; ω_s is the blood perfusion after the occlusion is applied for a sufficiently long time, 60 s in the case of experiments here; ω_{max} is the maximum hyperemic blood flow; τ_0 is a time constant depicting the falling speed of blood flow after occlusion is applied; t_{dw} is the time required to reach the maximum hyperemic blood flow after the release of occlusion; τ_h indicates the rate at which the blood flow returns to the baseline value during the reperfusion; $t_{occ,st}$ and $t_{occ,end}$ denote the starting and ending times of the occlusion, respectively. Except for $t_{occ,st}$ and $t_{occ,end}$, which are known in experiments ($t_{occ,st}$=300 s, $t_{occ,end}$=360 s), there are six parameters in this model of reactive hyperemia which can be varied to simulate the temperature history of blood perfusion. The aim of the thermal analyses is to obtain an optimized set of parameters that can best match the experiment data of temperature-time profile at the skin surface right above the artery. Note that the baseline blood flow ω_0 does not involve the occlusion process, and thus it can be determined using the temperature value measured before the occlusion (Stage I). The blood flow ω_s and time parameter τ_0 (only related to Stage II) are determined by the measured temperature-time profile during Stage II, and the other three parameters (ω_{max}, t_{dw} and τ_h,) are determined by the experimental data during Stage III. Besides the baseline flow rate (ω_0), there are five parameters in our simulations, i.e., $\alpha=\omega_s/\omega_0$, $\beta=\omega_{max}/\omega_0$, τ_0, t_{dw} and τ_h, whose ranges are listed in Supplementary Table 1, based on reported experiments[7,8].

Finite element analyses (FEA) were carried out to solve the transient heat transfer equation, and determine the temperature distribution numerically. 4-node linear heat transfer elements were used, and refined meshes were adopted to ensure the accuracy. The boundary conditions include the heat convection at the artery wall with blood flow of body temperature (the effective heat transfer coefficient was given by Eq. (7)), and the natural convection at the outer surface of skin with air of room temperature. The geometric and thermal-physical properties of various tissues are given in Supplementary Table 2. For the reactive hyperemia model described above, the parameters of blood flow are determined by numerical calculations as ω_0=15 mL/min (9.8 cm/s using a vessel diameter of 1.8 mm), ω_s=3 mL/min, ω_{max}=150 mL/min (98 cm/s), τ_0=5 s, t_{dw}=15 s, τ_h=45 s. For this set of parameters, the temperature-time profile obtained from FEA agrees reasonably well with the experiment results (Fig. 4d). The temperature distributions in the tissues are demonstrated in Supplementary Figure S11 for four typical stages before and after the occlusion, which clearly shows that the heating effect localizes nearby the artery and decreases rapidly away from the artery.

Supplementary Note 10: Transient plane source analysis

Thermal conductivities of skin are determined using the transient plane source (TPS) analysis[9,10] in an iterative, empirical fashion. The plane sources in this case are the individual square elements of the TCR device. The experiment consists of a 6 second measurement procedure as described in the Methods, with 2 s of heating at with 1.5 mA applied current, which generates 2 mW of power in the 1 mm x 1 mm square element. The temperature rise in the TCR element during heating is measured in the same fashion as in all experiments presented here, by measuring the voltage drop with a known applied current. The transient heating of a square plane has been shown to follow

$$\overline{\Delta T}(\tau)=\frac{P_0}{4a\pi^{1/2}k}H(\tau) \tag{9}$$

Where P_0 is the power output from the TCR element and approximated as constant during heating due to the <2% resistance change during heating, 2a is the width of the heater square (a = 0.5 mm in this case), k is the thermal conductivity, ΔT is the average temperature rise in the heater, τ is given by

$$\tau=\left(\frac{\alpha t}{a^2}\right)^{1/2} \tag{10}$$

where α is the thermal diffusivity of the medium, and $H(\tau)$ is given by

$$H(\tau) = \int_0^{\tau} dv \left\{ \operatorname{erf}(v^{-1}) - \pi^{-1/2} v [1 - \exp(-v^{-2})] \right\} \tag{11}$$

where τ is solved iteratively to generate a linear relation of $\Delta T(\tau)$ with $H(\tau)$, where $H(\tau)$ is solved numerically. Thermal conductivity, k, is then determined from this relation.

In our studies, deionized water is used as a calibration medium of known thermal conductivity (0.6 $W \cdot m^{-1} \cdot K^{-1}$) to generate an effective length value for a, which is then used in all subsequent measurements to determine thermal conductivity. The determination of an effective length allows us to correct for geometrical differences from an ideal plane source, such as our serpentine wire structure and finite plane, as well as the presence of the silicone backing followed by air on the back of the sensor. It is also noted that the probing depth of the measurement is given as

$$\Delta_p = \beta (\alpha t_{max})^{1/2} \tag{12}$$

where β is a constant of approximately 1 and t_{max} is the time length of heating, which gives a probing depth of approximately 500 μm for our experiments here.

References

1 Sondheimer, E. H. The Mean Free Path of Electrons in Metals. *Adv Phys* **1**, 1-42 (1952).

2 Cohen, M. L. Measurement of Thermal-Properties of Human-Skin - Review. *J Invest Dermatol* **69**, 333-338 (1977).

3 Lu, C. F. *et al.* A thermal analysis of the operation of microscale, inorganic light-emitting diodes. *P Roy Soc a-Math Phy* **468**, 3215-3223 (2012).

4 Andrews, L. *Special Functions of Mathematics for Engineers (second edition)*. (SPIE Press, 1997).

5 Technical datasheet from manufacturer, Dupont Co.

6 Technical datasheet from manufacturer, PSC A/S.

7 Deshpande, C. *Thermal analysis of vascular reactivity* MS thesis, Texas A&M University, (2007).

8 Akhtar, M. W., Kleis, S. J., Metcalfe, R. W. & Naghavi, M. Sensitivity of digital thermal monitoring parameters to reactive hyperemia. *Journal of Biomechanical Engineering* **132** (2010).

9 Gustafsson, S. E. Transient plane source techniques for thermal conductivity and thermal diffusivity measurements of solid materials. *Review of Scientific Instruments* **62**, 797-804 (1991).

10 Rosenbaum, E. J. *Thermal properties and characterization of methane hydrates* M.S. thesis, University of Pittsburgh, (2001).

11 Fiala, D., Lomas, K. J. & Stohrer, M. A computer model of human thermoregulation for a wide range of environmental conditions: The passive system. *Journal of Applied Physiology* **87**, 1957-1972 (1999).

12 Song, W. J., Weinbaum, S., Jiji, L. M. & Lemons, D. A combined macro and microvascular model for whole limb heat transfer. *Journal of Biomechanical Engineering* **110**, 259-268 (1988).

13 Sieg, P., Hakim, S. G., Bierwolf, S. & Hermes, D. Subcutaneous fat layer in different donor regions used for harvesting microvascular soft tissue flaps in slender and adipose patients. *International Journal of Oral and Maxillofacial Surgery* **32**, 544-547 (2003).

14 Shen, H. *et al.* A genomewide scan for quantitative trait loci underlying areal bone size variation in 451 Caucasian families. *Journal of Medical Genetics* **43**, 873-880 (2006).

15 Shima, H., Ohno, K., Michi, K. I., Egawa, K. & Takiguchi, R. An anatomical study on the forearm vascular system. *Journal of Cranio-Maxillo-Facial Surgery* **24**, 293-299 (1996).

16 McCartney, C. J. L., Xu, D., Constantinescu, C., Abbas, S. & Chan, V. W. S. Ultrasound Examination of Peripheral Nerves in the Forearm. *Regional Anesthesia and Pain Medicine* **32**, 434-439 (2007).

17 Kathirgamanathan, A., French, J., Foxall, G. L., Hardman, J. G. & Bedforth, N. M. Delineation of distal ulnar nerve anatomy using ultrasound in volunteers to identify an optimum approach for neural blockade. *European Journal of Anaesthesiology* **26**, 43-46 (2009).

DOI: 10.1038/NMAT3755

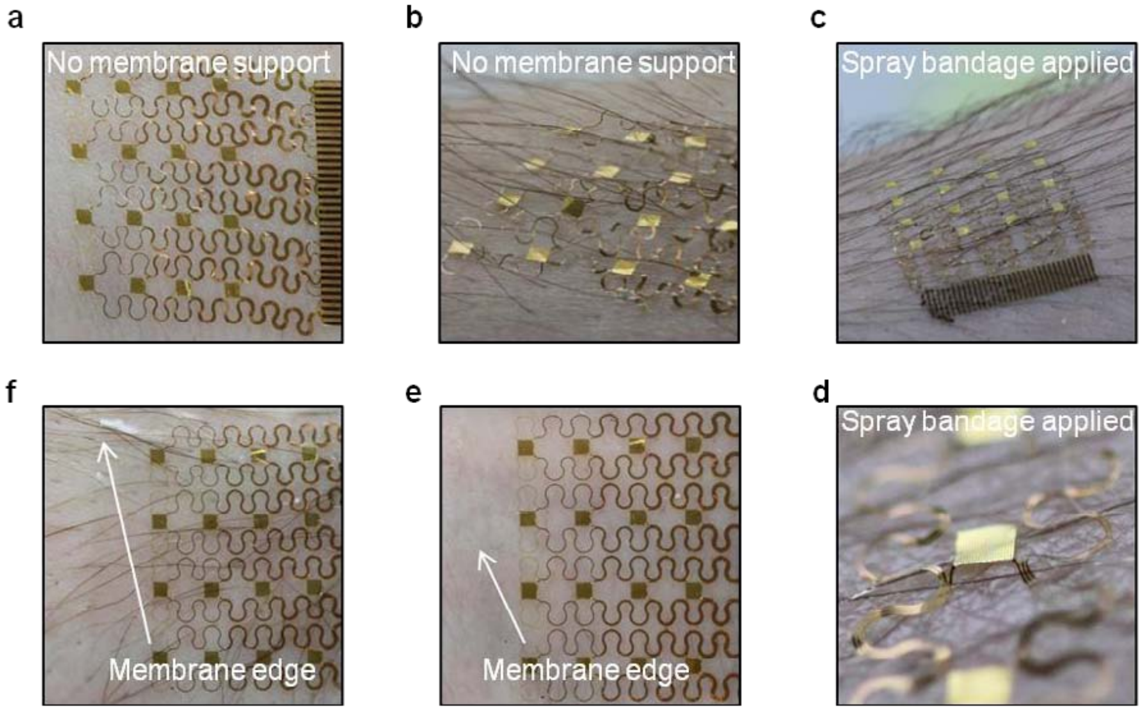

Supplementary Figure S1: Effects of hair on adhesion. (**a**) A 4x4 TCR array with no supporting membrane applied to an area of hairless skin. (**b**) An array with no supporting membrane applied to an area with significant hair. Some hair can rise between individual elements in the array, but adhesion is significantly frustrated. (**c**) An array with no supporting membrane applied to an area with significant hair following the application of commercial spray-on bandage. Adhesion is significantly improved; however hair directly beneath a sensor element may limit intimate thermal contact (**d**). (**e**) An array with a supporting silicone membrane applied to an area of hairless skin. (**f**) An array with a supporting silicone membrane applied to an area with significant hair. Here, the supporting membrane helps to flatten the hair, to allow for device adhesion.

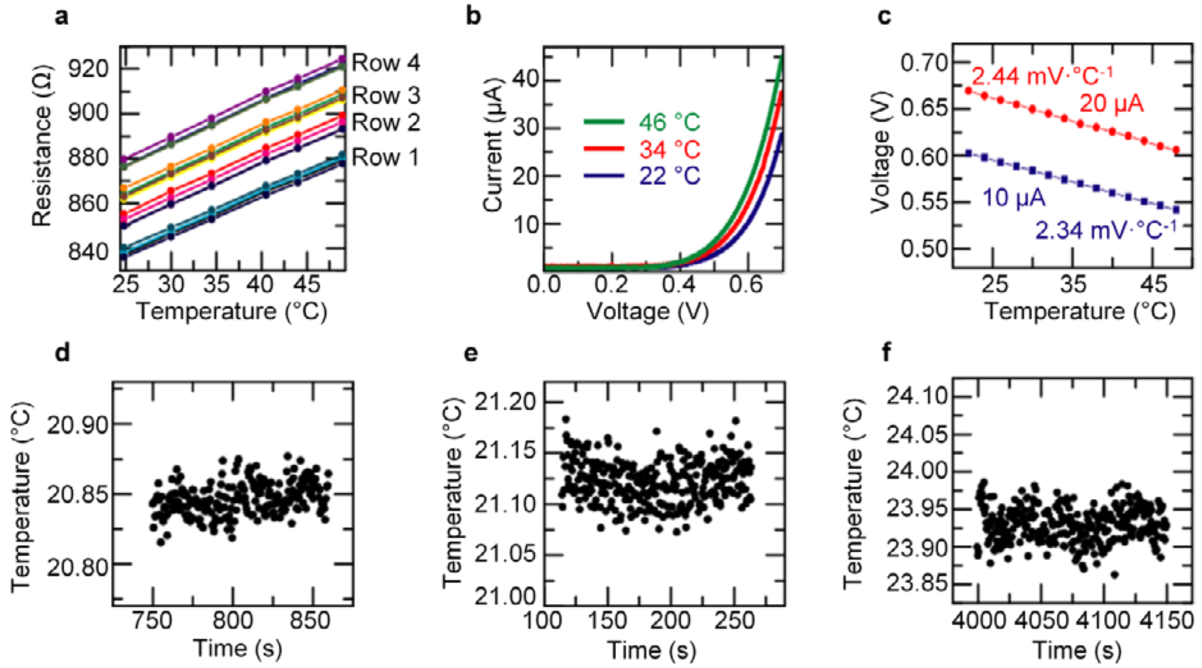

Supplementary Figure S2: Sensor calibration and noise measurements. (**a**) 4 x 4 TCR sensor array temperature calibration. Calibration curves appear in four groups of four sensors each, due the differing interconnect distances leading to each row of sensors. (**b**) Representative I-V curves of a single sensing element from a PIN device, at different temperatures. (**c**) Representative temperature calibration from single element of a PIN device at 10 µA (blue) and 20 µA (red). (**d**) Representative TCR device measurement at 2 Hz in air (std. dev = 0.012 °C) and (**e**) on skin (std. dev. = 0.021 °C). (**f**) Representative IR measurement at 2 Hz of skin (std. dev. = 0.024 °C, trend is removed).

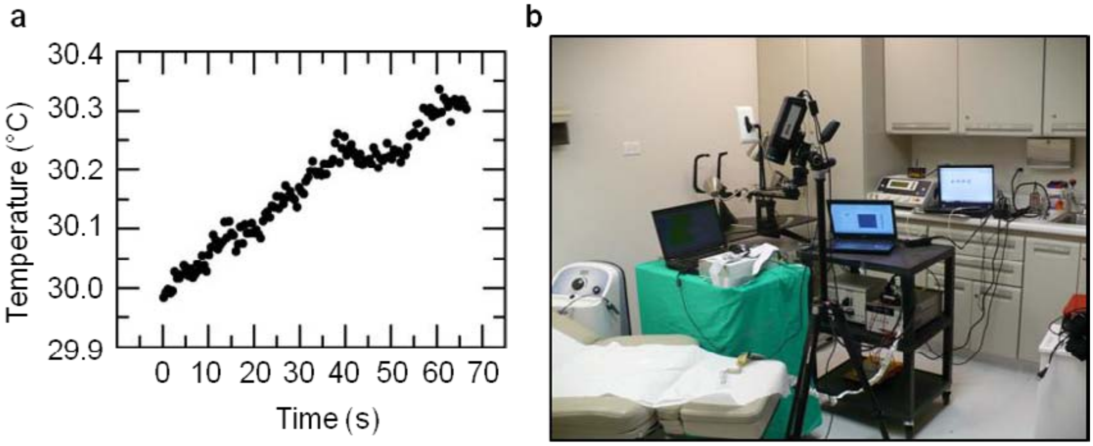

Supplementary Figure S3: Noise measurements in clinical exam room. (a) Temperature measurements on skin from a TCR array element taken in a clinical exam room at Northwestern Memorial Hospital in Chicago, IL (std. dev. = 0.023 °C, after linear trend is removed). Measurements were performed while simultaneously running many pieces of electrical equipment, beyond what is expected in a typical exam room, as shown in (**b**).

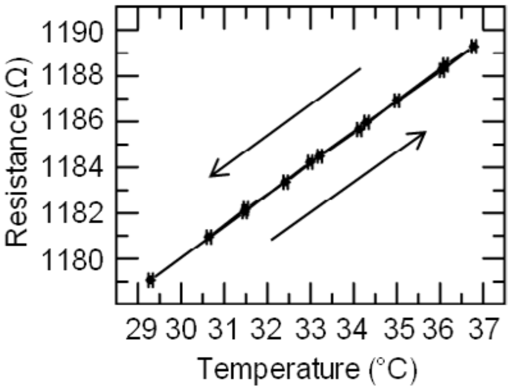

Supplementary Figure S4: Representative hysteresis of TCR array element. Resistance of a TCR array element as measured during a heating and cooling cycle on a hotplate (~0.5 °C/min heating, ~0.2 °C/min cooling). Temperature is determined using an IR camera. Data shows no hysteresis within the uncertainty of the measurement (<73 mK. IR camera sensitivity of 50 mK, as stated by manufacturer. TCR device sensitivity of 23 mK, as stated in main text). All measurements fall within 73 mK of a linear fit line, with points randomly scattered above and below the fit during both heating and cooling.

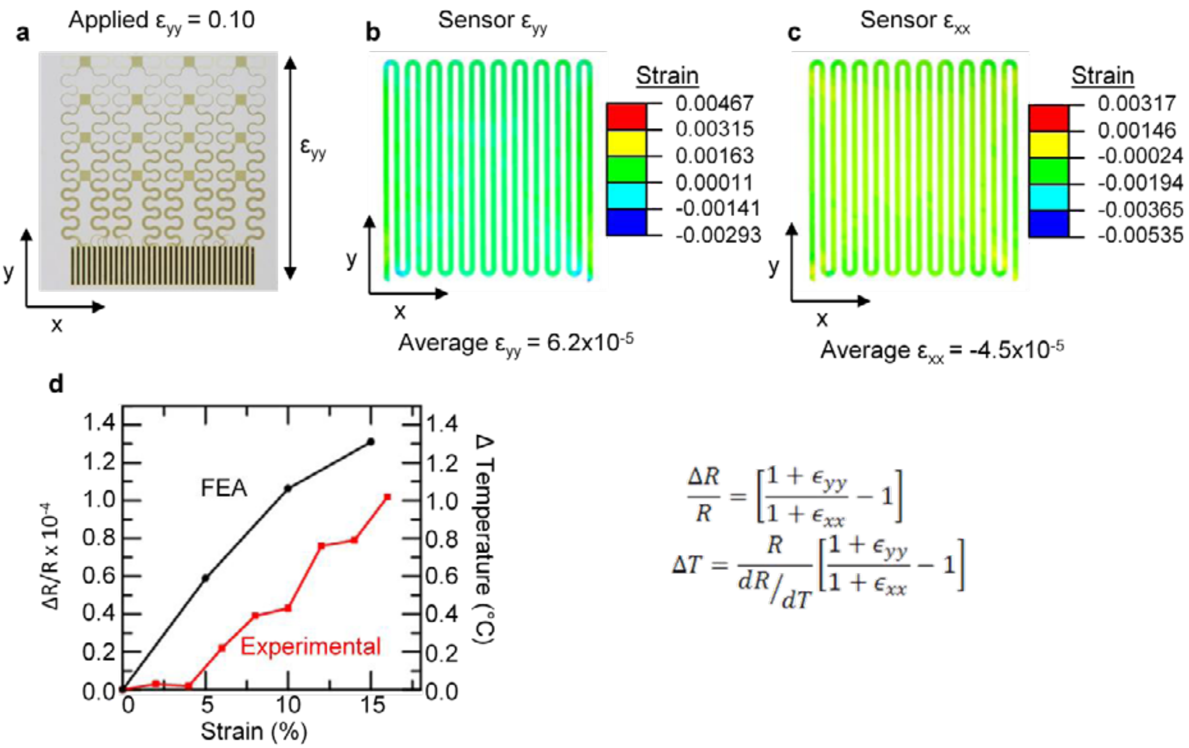

$$\frac{\Delta R}{R} = \left[\frac{1+\epsilon_{yy}}{1+\epsilon_{xx}} - 1\right]$$

$$\Delta T = \frac{R}{dR/_{dT}}\left[\frac{1+\epsilon_{yy}}{1+\epsilon_{xx}} - 1\right]$$

Supplementary Figure S5: Strain in TCR sensors. (**a**) Optical image of 4 x 4 TCR sensor array showing representative direction of applied strain. (**b**) FEA results of 10% applied strain in y-direction to substrate showing the resultant ε_{yy} strain distribution of a TCR sensor and (**c**) ε_{xx} strain distribution of a TCR sensor. (**d**) FEA (black) and experimental (red) results of applying strain to substrate in the y-direction, showing resistance change due to strain and resultant error in temperature reading.

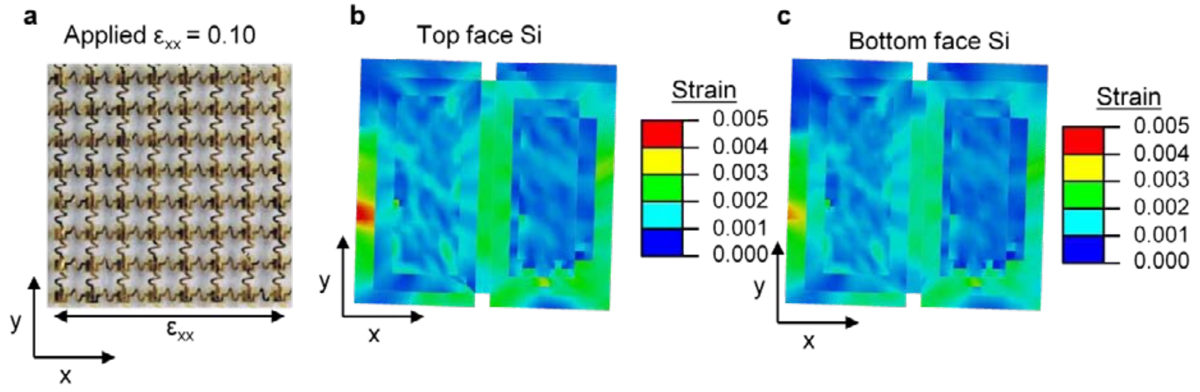

Supplementary Figure S6: Strain in PIN sensors. (**a**) Optical image of 8 x 8 PIN sensor array showing representative direction of applied strain. (**b**) FEA results of 10% applied strain in x-direction to substrate showing the resultant top surface Si strain distribution of a PIN sensor and (**c**) bottom surface Si strain distribution of a PIN sensor.

DOI: 10.1038/NMAT3755

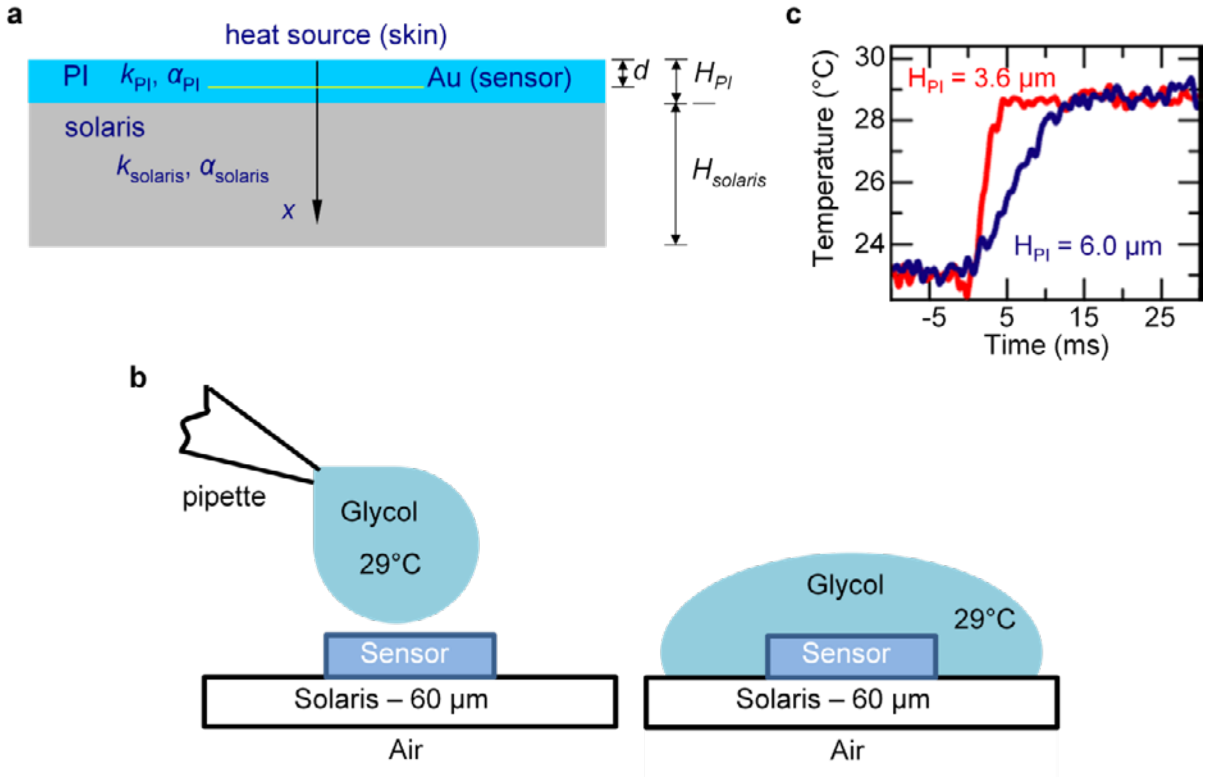

Supplementary Figure S7: Sensor response time. (**a**) Layers used in analytical modeling to determine sensor response time on skin. (**b**) Experimental setup for measuring sensor response time. A warm drop of ethylene glycol, which has similar thermal properties to skin, is dropped onto the sensor. (**c**) Experimental sensor response time to warm glycol droplet. The time required for the sensor to reach 90% of the total temperature change is 3.7 ms and 13.1 ms for the case of H_{PI} = 3.6 μm and H_{PI} = 6.0 μm, respectively.

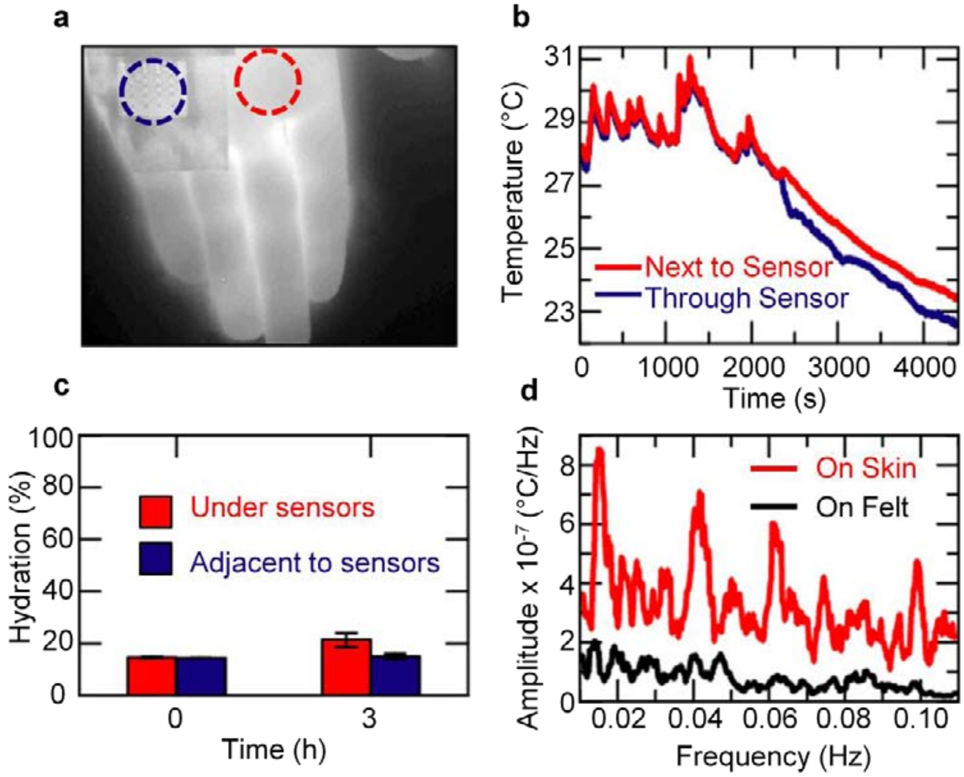

Supplementary Figure S8: Effects on physiology. (**a**) IR image showing locations used for comparison temperature data. (**b**) Comparison of IR temperature data through the TCR device (red) and next to the TCR device (blue) obtained during a mental stimulus experiment. (**c**) Skin hydration changes after wearing TCR device for 3 hours as measured by commercial Delfin Moisture Meter. (**d**) Comparison of frequency power spectrum measured by TCR device during 1 hour on skin (red) and a felt pad (black).

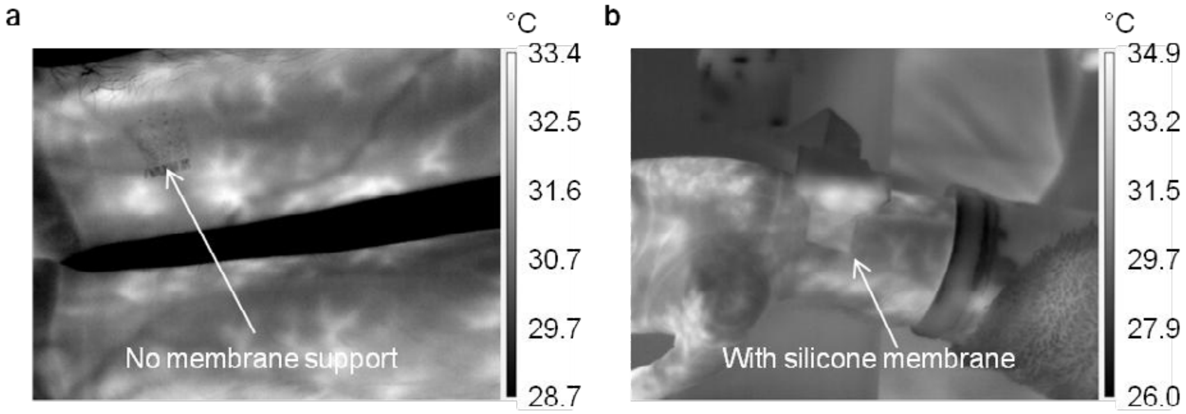

Supplementary Figure S9: Effect on skin temperature during profuse sweating. IR images of forearm during profuse sweating immediately following high-intensity aerobic exercise while wearing (**a**) a device with no supporting silicone membrane, and (**b**) a device with a thin silicone membrane substrate. The device with no silicone membrane (**a**) does not appear to have any effect on local skin temperature, while the device with a silicone membrane (**b**) causes a ~2 °C rise in temperature directly beneath the membrane, as compared to adjacent skin.

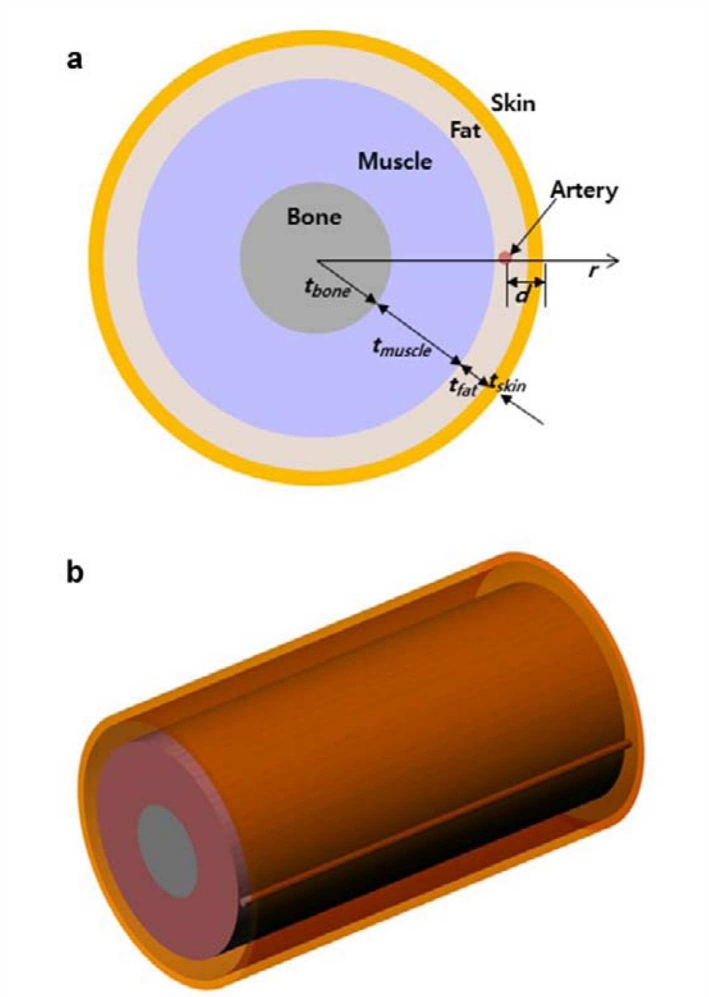

Supplementary Figure S10: Schematic illustration of the wrist model for simulations: (**a**) the cross-sectional view. (**b**) three-dimensional view.

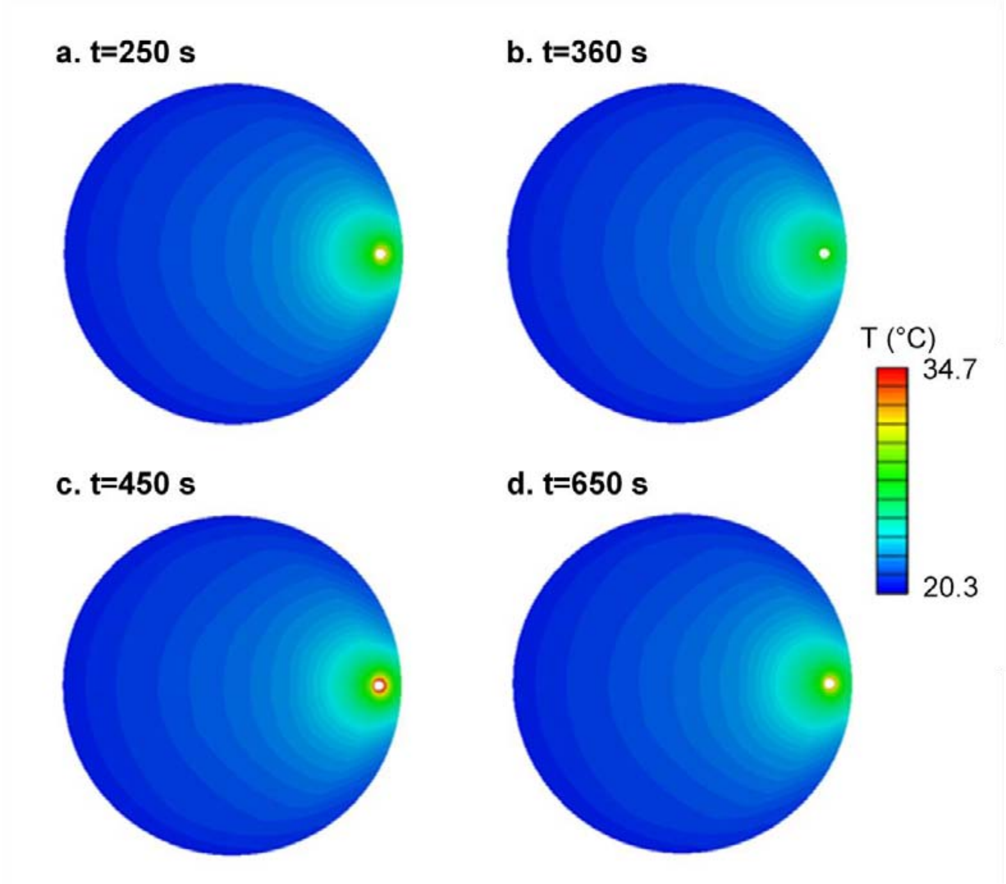

Supplementary Figure S11: FEA results on the temperature distribution in the tissues of blood flow model at four typical stages: (a) t=250 s, before occlusion. **(b)** t=360 s, at the release of occlusion. **(c)** t=450 s, when the temperature of skin surface is close to its maximum value. **(d)** t=650 s, when the temperature nearly returns to the baseline level after the occlusion.

Supplementary Table 1. The parameter range in the model of reactive hyperemia for simulations.

	$\alpha=\omega_s/\omega_0$	$\beta=\omega_{max}/\omega_0$	τ_0(s)	t_{dw} (s)	τ_h(s)
Range	[0, 0.20]	[2, 10]	[1, 5]	[15, 45]	[45, 80]

Supplementary Table 2. The geometric and thermal-physical properties of various tissues for the wrist, where *t* denotes the thickness, *D* is the diameter of the artery, and *d* is the depth of the artery.

Parameter	Skin	Fat	Muscle	Bone	Blood
ρ (kg/m^3)[7,11]	1085	850	1085	1357	1069
c_p (J/kg/K)[7,11]	3680	2300	3768	1700	3659
k (W/m/K)[7,11]	0.47	0.16	0.42	0.75	/
t (mm)[12-14]	1.0	4.4	13.6	10.0	/
D (mm)[15]	/	/	/	/	1.8
d (mm)[16,17]	/	/	/	/	4.0